The intergalactic medium near high-redshift galaxies

Rakic, O.

4

Measuring Galaxy Halo Masses from the Surrounding Lyα Absorption Distribution

We measure dark matter halo masses of $\langle z \rangle \approx 2.36$ star-forming galaxies by matching the observed H I Lyα absorption distribution around them, as observed in the spectra of background QSOs, to the absorption around haloes above a given mass in the SPH cosmological simulations. The implied minimum halo mass, $\log_{10} M_{\rm min} / \, {\rm M}_{\odot} = 11.6^{+0.20+0.50}_{-0.20-0.60}$, is in good agreement with the mass estimates from clustering analysis. To test the robustness of the method, we employ a simulation with WMAP1 cosmological parameters, as opposed to the WMAP3 parameters used for the rest of the simulations in our study, and find that it gives results consistent with our reference model. A simulation with a highly efficient AGN feedback implementation implies masses slightly higher, but consistent with those inferred from simulations with weaker feedback. A particularly strong point of this method is that it can be used in narrow field galaxy-QSO surveys, i.e. $\approx 30 \times 30$ arcseconds. In addition, we find that the recently observed redshift space distortions, presented in Chapter 3, in the 2-D H I Lyα absorption distribution are a consequence of large-scale gas infall into potential wells occupied by galaxies.

4.1 Introduction

THE mass of the host dark matter halo is believed to be the most important factor that determines galaxy evolution. When it comes to the most massive structures in the Universe, the employed techniques for measuring halo mass include measurements of Sunyaev-Zeldovich effect (e.g. Sunyaev & Zeldovich 1972; Motl et al. 2005), cluster X-ray temperature and luminosity (e.g. Reiprich & Böhringer 2002), strong lensing (e.g. Gavazzi et al. 2007), weak lensing (also called galaxy-galaxy lensing; e.g. Kaiser & Squires 1993), and kinematics of galaxies (e.g. Zwicky 1937). Measuring dark matter halo masses of individual galaxies is more difficult and usually requires statistical methods such as already mentioned weak lensing (e.g. Mandelbaum et al. 2006), clustering analysis (e.g. Kaiser 1984), satellite kinematics (e.g. More et al. 2011), and abundance matching (e.g. Conroy et al. 2006), although Haas et al. (2011) found that the most popular environmental indicators (e.g. number of galaxies within a given distance, or distance to the Nth nearest neighbour) also strongly correlate with halo mass even for single galaxies but with a large scatter.

Weak lensing studies rely on measuring gravitationally induced tangential shear distortions of background galaxies around foreground galaxies. Even though the individual distortions are small, averaging over a large ensemble of galaxies allows statistical reconstruction of dark matter density distributions around a given galaxy population. This method has been very successful at estimating dark matter halo masses for low-redshift galaxies. However, it is not a viable method for high-redshift objects since lensing cross-section peaks half way towards background galaxy, and is thus very small at $z \geq 2$. Furthermore, the number of both foreground and background galaxies becomes too low for getting a sufficient statistical sample, and measuring shapes of galaxies becomes increasingly hard.

As known from structure formation studies, more massive dark matter haloes cluster more strongly, and on scales greater than the haloes the galaxies inhabiting such haloes cluster similarly. Matching the observed clustering properties of a given galaxy population with the clustering of haloes in N-body simulations leads to estimates of the most likely host halo masses. This method has facilitated some important insights into the properties of galaxies, and their likely descendants (e.g. Adelberger et al. 1998, 2005b; Quadri et al. 2007; Conroy et al. 2008).

In this chapter we measure galaxy halo masses from H I Lyα absorption profiles. Numerous studies have shown that the absorption of the light from a background object (e.g. QSO) is increased when the sightline passes near a foreground galaxy (e.g. Chen et al. 1998, 2001; Penton et al. 2002; Adelberger et al. 2003, 2005; Crighton et al. 2010; Prochaska et al. 2011; Rakic et al. 2011), and at high-redshift this enhancement can be statistically detected out to distances of several proper Mpc (pMpc). Kim & Croft (2008) found that

such absorption profiles can be used to measure halo masses of foreground QSOs and galaxies by comparing them to mock observations from smoothed particle hydrodynamics (SPH) simulations. Somewhat related to this method is also work of Faucher-Giguère et al. (2008) who found that the Lyα optical depth statistics in the QSO proximity zones depends on dark matter halo masses of the QSO hosts. In comparison with previous studies we use higher resolution SPH simulations, and more models with varied galactic feedback prescriptions.

We apply the method to the observed Lyα absorption distribution around galaxies at $\langle z \rangle \approx 2.36$ from Rakic et al. (2011). They study the intergalactic matter distribution around rest-frame UV selected star-forming galaxies through the analysis of the absorption spectra of background QSOs, and find enhanced Lyα absorption within ≈ 3 pMpc from galaxies. They also present a 2-D (i.e. along the line of sight, LOS, and in the transverse direction) absorption distribution where they measure a slight compression of signal along the LOS on scales $\gtrsim 1.5$ pMpc. This compression suggests large-scale infall of gas into the potential wells occupied by the galaxies.

This observational study is particularly suitable for testing the method because the dark matter halo masses of their galaxies are already known from clustering analyses (e.g. Adelberger et al. 2005b; Conroy et al. 2008, Trainor et al., 2011, in preparation). Conroy et al. (2008) found that every halo at $z \sim 2$ with $M_{\rm h} > 10^{11.4} h^{-1} M_{\odot}$ hosts a star-forming galaxy from the photometric sample out of which the galaxies used in Rakic et al. (2011) were drawn. This result was obtained using N-body simulations with the WMAP1 cosmology. Using the WMAP3 cosmology (which is what the simulations in this paper are based on) they found a 0.3-0.4 dex smaller minimum halo mass. Using a spectroscopic sample, almost identical to the one used by Rakic et al. (2011), Trainor et al. (2011, in preparation) found that these galaxies reside in halos with $M_{\rm h} > 10^{11.75} h^{-1} M_{\odot}$, using WMAP1 cosmological parameters.

We describe the simulations in Section 4.2. Our halo mass measuring method is presented in Section 4.3. We explain the observed redshift space distortions seen in the 2-D absorption maps from Rakic et al. (2011) in Section 4.4. We conclude in Section 4.5. Proper distances throughout the text are denoted as pMpc, and comoving as cMpc. When a quantity is not expressed in terms of h (e.g. when stating distances), the value of h from the appropriate set of cosmological parameters is assumed.

4.2 Simulations

We use a subset of simulations from the suite of OverWhelmingly Large Simulations (OWLS; Schaye et al. 2010). The simulations were run using a modified version of GADGET-3 (last described in Springel 2005), which is a Lagrangian SPH code. These simulations include star formation (Schaye & Dalla Vecchia 2008), supernova (SN) feedback (Dalla Vecchia & Schaye

2008), radiative heating and cooling via 11 elements (hydrogen, helium, carbon, nitrogen, oxygen, neon, magnesium, silicon, sulphur, calcium, and iron) in the presence of the cosmic microwave background and the Haardt & Madau (2001) model for the ionizing background radiation from galaxies and quasars (Wiersma et al. 2009a), and chemodynamics (abundances of elements released by type Ia and type II SNe, stellar winds, and asymptotic giant branch stars; Wiersma et al. 2009b). The assumed initial mass function (IMF) is that of Chabrier (2003), with stars ranging in mass from 0.1 to 100 $M_{\odot}$. Box sizes and (the initial) baryonic and dark matter particle masses of the simulations used here are specified in Table 4.1. The cosmological parameters used in the simulations are from the Wilkinson Microwave Anisotropy Probe (WMAP) 3-year results (Spergel et al. 2007), $\{\Omega_{\rm m}, \Omega_{\rm b}, \Omega_{\Lambda}, \sigma_8, n_{\rm s}, h\} = \{0.238, 0.0418, 0.762, 0.74, 0.951, 0.73\}$.

We use the 'reference' (*REF*) model, model with AGN feedback (*AGN*), model using 'Millennium cosmology' (*MILL*), and a model with a different SN feedback prescription (*WML4*). All of the models are described in detail by Schaye et al. (2010); here we provide only short descriptions.

The *REF* and the *AGN* models are almost identical, except that the latter includes prescriptions for the growth of supermassive black holes and for AGN feedback. The AGN feedback implementation is a modified version of that of Springel (2005), and is described in Booth & Schaye (2009). It involves black holes injecting 1.5 % of the rest-mass energy of the accreted gas, in the form of heat, into the surrounding matter. Booth & Schaye (2009, 2010) show that this efficiency results in excellent agreement with the observed, $z = 0$, scaling relations between black hole masses and the properties of their host galaxies. We chose this simulation to test the effect of extreme feedback on our results as we expect that it could potentially influence physical properties (e.g. density and temperature) of the absorbing gas near galaxies.

To test the effect of 'cosmology', and to facilitate comparisons with previous studies that used older estimates of the cosmological parameters, we employ the 'Millennium cosmology' (Springel et al. 2005) in our *MILL* simulation. The *MILL* simulation uses the cosmological parameter values $\{\Omega_{\rm m}, \Omega_{\rm b}, \Omega_{\Lambda}, \sigma_8, n_{\rm s}, h\} = \{0.25, 0.045, 0.75, 0.9, 1.0, 0.73\}$. As found by Conroy et al. (2008), the lower values of σ_8 that are implied by more recent WMAP results cause the lower mass dark matter haloes to cluster more strongly than in models with higher σ_8. Hence the minimum mass of haloes implied by the observed clustering of a galaxy population is lower. The faster growth of structure in the *MILL* simulation also causes higher predicted global star-formation rate (SFR) densities, and thus the mass loading factor in the *MILL* model for the SN driven winds is doubled in comparison with the *REF* model, to $\eta = 4$. This is done in order to match the observed peak in the star-formation history (SFH). We note that the latest, WMAP year 7, estimates of cosmological parameters (Komatsu et al. 2011), $\{\Omega_{\rm m}, \Omega_{\rm b}, \Omega_{\Lambda}, \sigma_8, n_{\rm s}, h\} = \{0.272, 0.0455, 0.728, 0.81, 0.967, 0.704\}$,

Table 4.1 – Relevant information for 50 and 100 h^{-1} cMpc simulation boxes used here. The columns give the comoving size of the box L, the total number of particles per component N (dark matter and baryons), the initial baryon particle mass $m_{\rm b}$, the dark matter particle mass $m_{\rm dm}$, and the maximum gravitational softening length.

Simulation	L $[h^{-1}\mathrm{cMpc}]$	N	$m_{\rm b}$ $[h^{-1}\,\mathrm{M}_\odot]$	$m_{\rm dm}$ $[h^{-1}\,\mathrm{M}_\odot]$	Soft. length $[h^{-1}\mathrm{ckpc}]$
L050 N512	50	512^3	1.1×10^7	5.1×10^7	1
L100 N512	100	512^3	8.7×10^7	4.1×10^8	2

have σ_8 value that is in between those from WMAP year 1 and WMAP year 3 results, while the value for Ω_m is closer to that from WMAP1.

WML4 is almost identical to the *REF* model, but the mass loading factor is the same as in the *MILL* simulation, which allows us to separate the effects of cosmological parameters and feedback prescriptions in our models.

4.2.1 Extracting sightlines from the simulations

We use only the $z = 2.25$ snapshot, as this is close to peak in the redshift distribution of the galaxy sample used in Rakic et al. (2011, $z \approx 2.36$), and the snapshots of the simulations are saved every $\Delta z = 0.25$. The observed galaxies cover the redshift range from $z \approx 2-2.8$, and we leave for future work the estimate of uncertainty in our results arising due to possible evolution from $z = 2.8$ to $z = 2$.

The masses and locations of the dark matter haloes in the simulations are determined using a spherical overdensity criterion as implemented in the SubFind algorithm (Dolag et al. 2009). SubFind finds the radius, r_{200}, and mass, m_{200}, of a spherical halo centered on the potential minimum of each identified halo, so that they contain a mean density of 200 times the critical density of the Universe at a given redshift.

We extract 12,500 sightlines within 5 pMpc from the halo centers, drawing haloes above a given mass limit randomly (which ensures that we sample the halo mass function correctly). This is done for 20 cases where we vary the minimum halo mass, $M_{\rm min}$, in steps of 0.1 dex in the range $M_{\rm min} = 10^{10.5} - 10^{12.5}\,\mathrm{M}_\odot$. There are 500 sightlines for every 200 pkpc impact parameter bin. Given that there are, e.g. $\sim 20,000$ haloes with mass above $10^{11}\,\mathrm{M}_\odot$, or ~ 700 haloes with mass higher than $10^{12}\,\mathrm{M}_\odot$ in a 100 h^{-1} cMpc box (see Figure 4.1 for number densities of haloes above a given mass), in most distance bins a single halo features only once. In addition, sightlines are always parallel to the box sides, but the axis is chosen randomly.

By setting only the minimum halo mass we implicitly assume that each halo above a given mass limit is a host to a galaxy from the observed population. We do not set the upper limit on halo mass because there is no upper

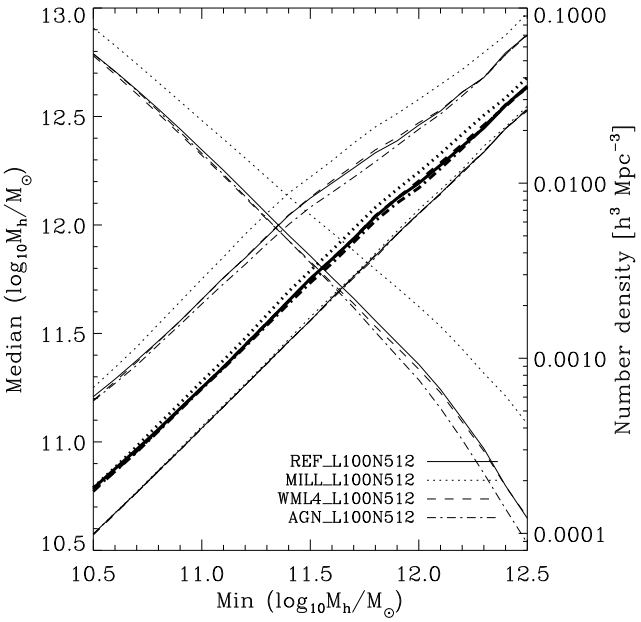

Figure 4.1 – Median halo mass above a given minimum halo mass (rising thick black curves), for different models, as measured from 100 h^{-1} cMpc boxes, with the 15.9th and 84.1th percentile (thin black rising curves above and below the median curves). The declining curves show the corresponding number density of haloes above a given minimum mass (right y-axis).

limit on the galaxy luminosity in the observed sample. Objects that are potentially missed by the selection based on rest-frame UV colors, e.g. massive red galaxies identified through their rest-frame optical colors (e.g. Franx et al. 2003), have space density smaller by more than an order of magnitude than the rest-frame UV selected galaxies used here, and are expected to have little impact on our statistics. In fact, we verified that using overlapping bins in halo mass with the specified minimum and maximum mass spaced by 1 dex yields very similar results to setting only the lower mass limit. This is due to the shape of the halo mass function, where the typical (median) mass above a given mass limit is only 0.2-0.3 dex higher than the set minimum (Figure 4.1).

The procedure for calculating absorption spectra is described in Appendix A4 of Theuns et al. (1998). QSO spectra from Rakic et al. (2011) were taken with Keck I/HIRES (Vogt et al. 1994) and have spectral resolution of FWHM $\approx 8.5\,\mathrm{km\,s^{-1}}$. We convolved our simulated spectra with a Gaussian with a FWHM $= 6.6\,\mathrm{km\,s^{-1}}$, and rebin to $1.4\,\mathrm{km\,s^{-1}}$ pixels. We do not expect the slightly higher resolution in the simulated spectra to have impact

on our results. We add Gaussian noise with a signal to noise (S/N) ratio of 100 to the spectra, to match the typical S/N from the observations.

The optical depth of all pixels from simulated spectra, with original median optical depth of $\log_{10}\tau_{\mathrm{Ly}\alpha} = -1.32$ (for randomly extracted sightlines), is scaled to match the median absorption level in the observed spectra, $\log_{10}\tau_{\mathrm{Ly}\alpha} = -1.28$ (Rakic et al. 2011). This is justified because of the large uncertainties in the intensity of the ionizing background radiation.

4.3 Measuring halo masses

In this section we show the results of matching 2-D H I Lyα absorption maps, 1-D cuts through such maps, and radially averaged absorption profiles to those from the simulations.

4.3.1 Resolution tests

The *REF* model was run in 25, 50, and 100 h^{-1}cMpc boxes, while the rest of the simulations are only available in 25 and 100 h^{-1}cMpc boxes. The smallest box size does not have sufficient high-mass haloes and is therefore not suitable for our study. The 50 h^{-1}cMpc simulation box samples the full range of the mass function well, and for the *REF* model we used this box size to test convergence and resolution by comparing it with the results of the 100 h^{-1}cMpc box. The latter samples the high end of the mass function well, but resolves haloes with e.g. $M_{\mathrm{h}} = 10^{10.5}\,\mathrm{M}_{\odot}$ with less than 10^2 dark matter particles (for the simulation with 512^3 particles), which is insufficient to get reliable results for such objects. However, comparison of the *REF* model with observations suggests that the most relevant mass range is $M_{\mathrm{h}} > 10^{11}\,\mathrm{M}_{\odot}$, which means that using 100 h^{-1}cMpc simulation boxes is appropriate for our particular problem. We show convergence tests in the Appendix.

4.3.2 Measuring halo mass from 2-D absorption maps

Figure 4.2 shows the observed Lyα 2-D absorption map in the top panel and the maps from simulations for the minimum halo masses of $M_{\mathrm{min}} = 10^{10.5}$, $10^{11.5}$, and $10^{12.5}\,\mathrm{M}_{\odot}$, in the bottom panels from left to right respectively. The distance bins in these maps are logarithmically spaced by 0.15 dex, both in transverse direction and along the LOS. We added errors to simulated galaxy redshifts, to mimic those from the observations (Steidel et al. 2010): to a random 10% subsample of simulated redshifts we added errors with $\sigma = 60\,\mathrm{km\,s^{-1}}$ (mimicking errors in redshifts measured from nebular emission lines), and to the remaining 90% of redshifts $\sigma = 125\,\mathrm{km\,s^{-1}}$ (imitating errors measured from rest-frame UV absorption and emission lines). It is evident that haloes with $M_{\mathrm{h}} > 10^{10.5}\,\mathrm{M}_{\odot}$ produce too little absorption to account for the observed absorption maps, while the more massive haloes, $M_{\mathrm{h}} > 10^{12.5}\,\mathrm{M}_{\odot}$, produce too much absorption at large impact parameters.

The middle panel, showing absorption near haloes with the minimum mass of $M_{\rm h} > 10^{11.5}\,{\rm M}_{\odot}$, resembles the observed distribution the most. The observed map is noisier, however, which is not surprising given that hundreds of sightlines contribute to each bin in simulated maps, as compared to ≈ 10 in the innermost bins of the observed map. None of the simulated maps shows enough absorption very close to galaxies (impact parameters $b \lesssim 100$ pkpc). Steidel et al. (2010) find that the absorption strength keeps rising closer to galaxies using their galaxy-galaxy pairs observations where the $b < 100$ pkpc region is sampled well, which suggests that there is probably a true deficiency of high column gas close to galaxies in the simulations, and that the discrepancy is not only a result of small number statistics (there are only 15 galaxies in the first, and 8 in the second impact parameter bin of Rakic et al. 2011). We will come back to this question in more detail below.

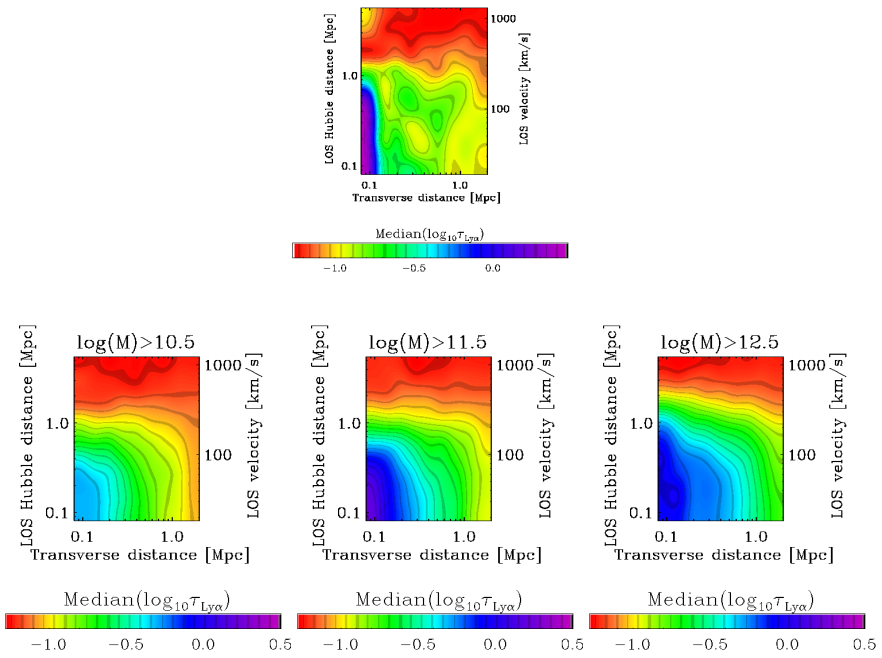

Figure 4.2 – Median 2-D distribution of Lyα absorption signal near haloes with, from left to right, $M_{\rm min} > 10^{10.5}, 10^{11.5}$ and $10^{12.5}\,{\rm M}_{\odot}$ at $z = 2.25$ using the *REF* model. Redshift errors (as described in the text) were included. The observed map from Rakic et al. (2011, their Figure 6) is in the top panel. In comparison with the observed absorption map, the extent of absorption in the first panel is too small, while the third panel shows too much absorption at large impact parameters.

Figure 4.2 indicates the approximate mass range for host haloes to produce absorption comparable to the observations. More quantitatively, we estimate the minimum halo mass by minimizing the reduced χ^2 between the

observed 2-D Lyα absorption maps and maps from the simulations, taking into account errors on data points from observations. We use only regions of maps with LOS separations smaller than 616 km s^{-1} because the absorption signal is consistent with noise beyond this point (see Figure 4.2), and therefore these parts have no constraining power. Different distance bins in 2-D maps are uncorrelated in the transverse direction, but are correlated on scales of 200 km s^{-1} along the LOS (Chapter 3). We therefore use 1000 bootstrap realizations of the observed galaxy sample to estimate the errors on the halo mass, instead of using a $\Delta\chi^2$ criterion. For each bootstrap realization of the data, we find the implied minimum halo mass by comparing the resulting maps to the simulated maps, and then find the 1 and 2σ confidence intervals from the sample of bootstrap realizations. Given a grid of minimum halo masses spaced by 0.1 dex, the errors on halo masses sometimes take discrete values. In order to prevent errors with zero values, in cases where this happens we set the error to half the grid spacing, i.e. 0.05 dex, since we cannot determine errors to better than this value.

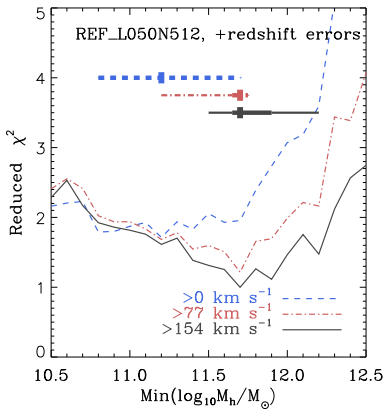

Figure 4.3 – The reduced χ^2 estimated by comparing the observed 2-D Lyα absorption map with the simulated maps for different minimum halo masses (x-axis), for the *REF* model in a 50 h^{-1} cMpc box. Given that regions close to galaxies are most affected by the uncertain baryonic physics and galaxy redshift errors, we show the resulting curves after using only absorbing regions separated by LOS velocity intervals greater than the values indicated in the legend. The curves show the results for the full sample. Their minima correspond to the best-fit minimum halo masses. The vertical rectangles show the median minimum halo masses as estimated from different bootstrap realizations. The thick horizontal lines show the 1σ confidence interval from bootstrap realizations, and the thin horizontal lines show the 2σ confidence intervals.

The dashed curves in Figures 4.3 and 4.4 show the reduced χ^2 from comparing absorption maps as a function of minimum halo mass used for simulated data. For the 50 h^{-1}cMpc *REF* simulation the implied mass is $\log_{10}M_{\rm min} = 11.2^{+0.5+0.5}_{-0.4-0.4}{\rm M}_\odot$, and for the 100 h^{-1}cMpc box it is $\log_{10}M_{\rm min} =$

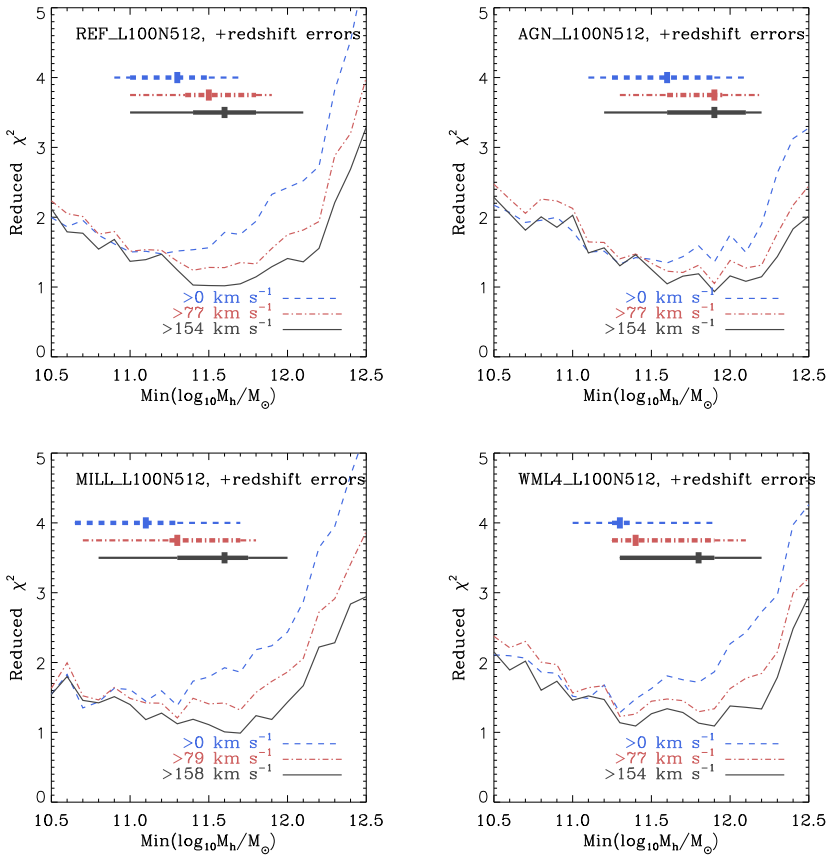

Figure 4.4 – Similar to Figure 4.3 but for more models simulated in 100 h^{-1} cMpc boxes (as opposed to 50 h^{-1} cMpc in the previous figure).

$11.2^{+0.3+0.5}_{-0.3-0.4}\,\mathrm{M}_\odot$ (the first and second pairs of errors indicate 1σ and 2σ confidence intervals, respectively). The two simulations give almost identical results, which justifies using larger boxes for the rest of the models.

Because uncertain baryonic physics and redshift errors could affect the absorption signal close to galaxies, we also compare parts of maps where these uncertainties are expected to have a smaller impact. We do so by excluding regions with $v_{\mathrm{LOS}} < 77$, and $154\,\mathrm{km\,s^{-1}}$ (separated by 0.3 dex in logarithmic space), or $v_{\mathrm{LOS}} < 79$ and $158\,\mathrm{km\,s^{-1}}$ for the *MILL* model (due to different cosmological parameters the same proper distance corresponds to different velocity separation), where v_{LOS} is the line of sight velocity separation between absorbers and galaxies. The resulting minimum halo mass from such conservative comparisons is in all cases consistent with the one inferred by compar-

ing the complete maps. Given that the simulations seem to underproduce the level of absorption very close to galaxies in comparison with the observations (e.g. Figure 4.2), and given the uncertain baryonic physics in the vicinity of galaxies, we choose to compare absorption distributions from observations and simulations only at LOS velocity separations $v_{\rm LOS} > 154\,{\rm km\,s^{-1}}$ (which is comparable to the redshift errors in the galaxy sample) as our default case. This implies a minimum halo mass of $\log_{10}M_{\rm min} = 11.7^{+0.2+0.5}_{-0.05-0.2}{\rm M}_\odot$ using the 50 h^{-1}cMpc box, and $\log_{10}M_{\rm min} = 11.6^{+0.20+0.50}_{-0.20-0.60}{\rm M}_\odot$ using the 100 h^{-1}cMpc box.

4.3.2.1 The AGN, MILL and WML4 models

The minimum mass implied by comparison of observations with the *AGN* simulation is $\log_{10}M_{\rm min} = 11.9^{+0.20+0.30}_{-0.30-0.70}$ M$_\odot$. This is somewhat higher than mass inferred from the *REF* model ($\log_{10}M_{\rm min} = 11.6^{+0.20+0.50}_{-0.20-0.60}$ M$_\odot$), but still consistent within 1σ. McCarthy et al. (2011) found that AGN eject large amounts of gas from galaxies at $z \sim 2-3$ using this simulation, which is why we need to move to higher mass haloes to get high enough columns of neutral gas to account for the observed absorption. Nevertheless, given that results differ by only 0.3 dex even when using a model with such extreme feedback, we conclude that this halo mass measuring method is robust to changes in baryonic physics prescriptions.

To quantify the impact of cosmology on our results, we compare the *MILL* and *WML4* simulations, which differ mostly in terms of σ_8, which is 0.9 for the former, and 0.74 for the latter model. We find minimum masses of $\log_{10}M_{\rm min} = 11.7^{+0.05+0.30}_{-0.40-0.90}{\rm M}_\odot$ and $11.4^{+0.50+0.80}_{-0.1-0.10}{\rm M}_\odot$, for *MILL* and *WML4*, respectively. These estimates are consistent with the value implied by the *REF* model. The minimum halo mass for the *MILL* model, slightly higher than the one for *WML4*, has a large uncertainty on the lower side. In addition, Figure 4.4 shows that the χ^2 curve for this simulation where we exclude only regions with LOS separations $\leq 79\,{\rm km\,s^{-1}}$ gives results that are more consistent with the *WML4* model ($\log_{10}M_{\rm min} = 11.3^{+0.4+0.5}_{-0.05-0.6}\,{\rm M}_\odot$). The fact that *WML4* gives a result consistent with that for the *MILL* model suggests that the exact value of σ_8 does not make a large difference.

For comparison we show 2-D Lyα absorption maps for different models in Figure 4.5, for haloes with $M_{\rm h} > 10^{11.5}\,{\rm M}_\odot$. *AGN* model shows weaker absorption signal within ~ 100 kpc from galaxies in comparison with other models, and *WML4* shows less absorption relative to the *REF* model.

The implied minimum masses from all models are summarized in Table 4.2. It is clear that the statistical errors on the minimum halo mass, which are around 0.2-0.3 dex, are comparable to the systematic errors arising due to uncertainties in the physics important for galaxy formation, as inferred by using simulations with different feedback prescriptions and different cosmologies. This demonstrates the robustness of this method for

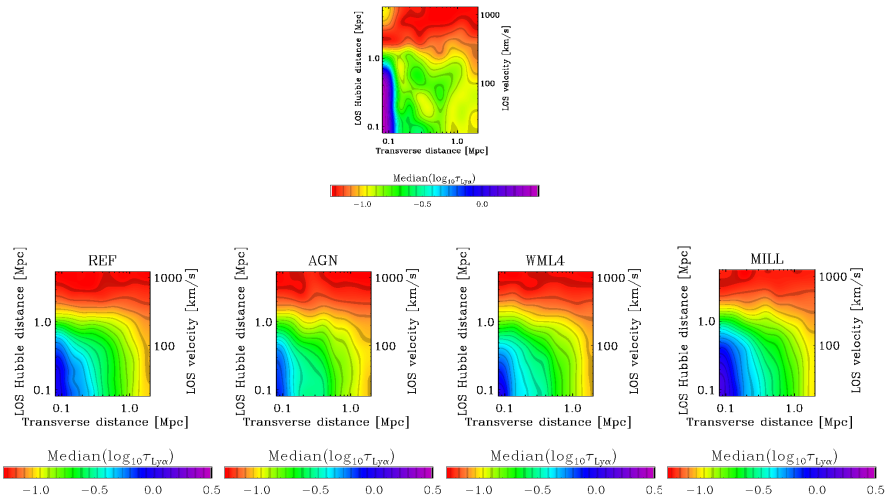

Figure 4.5 – Median 2-D distribution of Lyα absorption signal near haloes with $M_{\rm min} > 10^{11.5}$ at $z = 2.25$ using the *REF*, *AGN*, *WML4*, and *MILL* model, from left to right respectively. The observed map from Rakic et al. (2011, their Figure 6) is in the top panel.

Table 4.2 – The inferred minimum halo masses for different simulations are shown in the first column (with 1 and 2σ confidence intervals), while the corresponding number densities of haloes (and 1 and 2σ confidence intervals) as measured from the simulations with $100\,h^{-1}$ cMpc boxes are presented in the second column. For reference, the observed number density of galaxies in the photometric sample, from which objects in Rakic et al. (2011) were drawn for spectroscopic follow-up, is $11 \times 10^{-3}\,h^3\,{\rm Mpc}^{-3}$, with an uncertainty of 10% (Reddy et al. 2008). Galaxies in the spectroscopic sample are weighted toward brighter objects in comparison, and their number density is lower.

Models	Min. halo mass [$\log_{10}{\rm M}_\odot$]	n [$h^3\,{\rm Mpc}^{-3}$]
REF	$11.6^{+0.20+0.50}_{-0.20-0.60}$	$2.9^{+2.2+12.6}_{-1.2-2.2} \times 10^{-3}$
AGN	$11.9^{+0.20+0.30}_{-0.30-0.70}$	$1.0^{+1.6+7.3}_{-0.5-0.7} \times 10^{-3}$
MILL	$11.7^{+0.05+0.30}_{-0.40-0.90}$	$4.1^{+6.7+33.3}_{-0.5-2.1} \times 10^{-3}$
WML4	$11.4^{+0.50+0.80}_{-0.10-0.10}$	$4.7^{+1.5+1.5}_{-3.5-4.3} \times 10^{-3}$

measuring halo masses.

4.3.2.2 Number densities of haloes

The number density of galaxies in the photometric sample, from which galaxies in Rakic et al. (2011) were drawn, is $11 \times 10^{-3}\,h^3\,{\rm Mpc}^{-3}$, with an uncertainty of 10% (Reddy et al. 2008). The largest weights for spectroscopic follow-up were given to objects in the apparent magnitude range $R = 23{-}24.5$

(Steidel et al. 2004), while the limit for the photometric sample is $R = 25.5$. In addition, objects near the QSO sightlines (i.e. within 1-2 arcminutes) were given extra weight. There are ~ 2.5 times more objects in the photometric sample for the limiting magnitude of $R = 25.5$, than for $R = 24.5$, and so the lower limit on the number density of galaxies in the spectroscopic sample is $\sim 4.5 \times 10^{-3}\, h^3\, \mathrm{Mpc}^{-3}$. The real number density of objects in the spectroscopic sample is somewhere in between, because a non-negligible fraction of objects with $R > 24.5$ also have a spectroscopic follow-up.

Number densities of haloes above a minimum mass inferred in the previous section using different models, are given in Table 4.2. Their values are $2.9^{+2.2+12.6}_{-1.2-2.2} \times 10^{-3}$, $1.0^{+1.6+7.3}_{-0.5-0.7} \times 10^{-3}$, $4.1^{+6.7+33.3}_{-0.5-2.1} \times 10^{-3}$, and $4.7^{+1.5+1.5}_{-3.5-4.3} \times 10^{-3}\, h^3\, \mathrm{Mpc}^{-3}$ (quoting 1 and 2 σ confidence intervals as estimated from the errors on the minimum halo mass), for the *REF*, *AGN*, *MILL* and *WML4* model, respectively. All the estimates, apart for *AGN*, are consistent with the observed number densities within 1σ, and *AGN* agrees with the observations within 2σ. The minimum halo mass for the *MILL* model is 0.1 dex higher than that for the *REF* model, and yet the number density is also somewhat higher, while we would naively expect the number density to be lower given the higher halo mass. This is due to higher value of σ_8 in the *MILL* model (0.9 as compared to 0.74), which causes faster growth of structure (see Figure 4.1). Number densities for the *AGN* model although very low in comparison with other models, are consistent with them due to the large uncertainty on the minimum halo mass estimate.

4.3.2.3 Comparison with estimates from clustering measurements

The latest estimates of halo masses of $z \sim 2$ star-forming galaxies were presented by Conroy et al. (2008) and Trainor et al. (2011, in preparation). As already mentioned in the introduction, using a clustering analysis Conroy et al. (2008) found the minimum halo mass to be $10^{11.55}\, \mathrm{M}_\odot$ using the WMAP1 cosmology, and 0.3-0.4 dex smaller (i.e. $10^{11.15} - 10^{11.25}\, \mathrm{M}_\odot$) using the WMAP3 cosmology (which is the default cosmology in our study), and quote an error of ± 0.2 dex. Our results for the models that use these cosmological parameters ($\log_{10} M_{\mathrm{min}} = 11.7^{+0.05+0.30}_{-0.40-0.90}\, \mathrm{M}_\odot$ for the *MILL* model, using WMAP1, and $11.4^{+0.50+0.80}_{-0.10-0.10} \mathrm{M}_\odot$ for the *WML4* model, using WMAP3), although consistent within errors with their results, are both slightly higher. This could be due to the fact that they used the correlation function measured from the photometric galaxy sample, while we use only the brighter spectroscopic sample. Adelberger et al. (2005b) found that brighter galaxies in their photometric sample cluster more strongly, and therefore likely reside in more massive haloes. Trainor et al. (2011, in preparation) measure masses of $10^{11.9}\, \mathrm{M}_\odot$ for the spectroscopic sample using WMAP1 cosmological parameters, i.e. higher by ~ 0.3 dex than result by Conroy et al. (2008) for the photometric sample. Given that our results when using both the WMAP1

and WMAP3 cosmological parameters are ~ 0.2 dex higher than those from Conroy et al. (2008), in line with the expectation for the brighter spectroscopic sample, we conclude that the two methods (i.e. clustering analysis and matching of the Lyα absorption profiles) give consistent results.

4.3.2.4 Relevance for future surveys

We demonstrated that comparisons of observed 2-D Lyα absorption maps around galaxies with maps extracted from cosmological SPH simulations can be used to measure halo masses of the galaxy population in question. Our observed QSO-galaxy fields typically span areas of $\approx 5 \times 7$ arcminutes with the QSO in the middle. Here we test the performance of our method for a limited survey area of only $\approx 30 \times 30$ arcseconds, which corresponds to a cut along the LOS through the first impact parameter bin of the above 2-D maps ($b \lesssim 130$ pkpc). Figure 4.6 shows that the implied minimum mass is $\log_{10} M_{\rm min} = 11.6^{+0.50+0.50}_{-0.05-0.05}$ M$_\odot$, which agrees very well with that inferred from a comparison of the full maps ($\log_{10} M_{\rm min} = 11.6^{+0.20+0.50}_{-0.20-0.60}$ M$_\odot$).

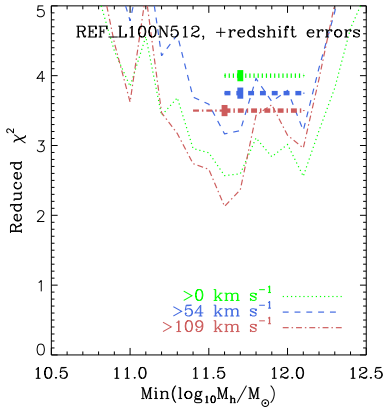

Figure 4.6 – The reduced χ^2 estimated by comparing the observed Lyα absorption profile through the first impact parameter bin of a 2-D map (i.e. cut along the LOS). The implied minimum mass agrees with the one indicated by comparison of full 2-D maps ($\log_{10} M_{\rm min} = 11.6^{+0.50+0.50}_{-0.05-0.05}$ M$_\odot$ as compared to the $11.6^{+0.20+0.50}_{-0.20-0.60}$ M$_\odot$, respectively).

This finding is relevant for future galaxy-QSO pair surveys such as the one planned with the VLT/MUSE integral field spectrograph (Bacon et al. 2010), whose field of view is 1×1 arcminute. Applying our method to MUSE observations will allow estimates of halo masses of Lyα emitters from a single telescope pointing on each QSO in the survey. This eliminates the need to make a wide field mosaic to measure clustering, which would in any case not be feasible for the faint objects dominating the number density of galaxies detected in the deep QSO fields.

4.3.3 Measuring mass from radially averaged absorption profiles

Comparing radially averaged absorption profiles to the ones from simulations yields results consistent with those implied by 2-D distributions but the confidence intervals are larger. This is not surprising given that here we average over the transverse and LOS signal, in which case we lose some constraining power in comparison with the 2-D map. Figure 4.7 shows the median $\log_{10}(\tau_{\mathrm{Ly}\alpha})$ as a function of distance from galaxy haloes, in 5 mass bins, with the observational results shown as gray symbols. The observed profile follows the one near haloes with $M_{\mathrm{h}} > 10^{11.5}\,\mathrm{M}_{\odot}$ the most closely. In this plot we see that the discrepancy at small impact parameters, where simulations underpredict the amount of absorption, is at the 2σ level. As mentioned above, Steidel et al. (2010) find that the absorption within 100 pkpc keeps rising, which suggests a true deficiency of high column density gas at small impact parameters. This could be explained if cold gas physics in the simulations is not captured sufficiently well (e.g. in reality gas at ISM densities can self-shield to form a cold phase with $T \ll 10^4$ K, while in the simulations its temperature stays at $\gtrsim 10^4$ K). Also, the SN feedback prescription in the *REF* model is possibly not fully appropriate and perhaps heats the gas near galaxies to higher temperatures than in reality.

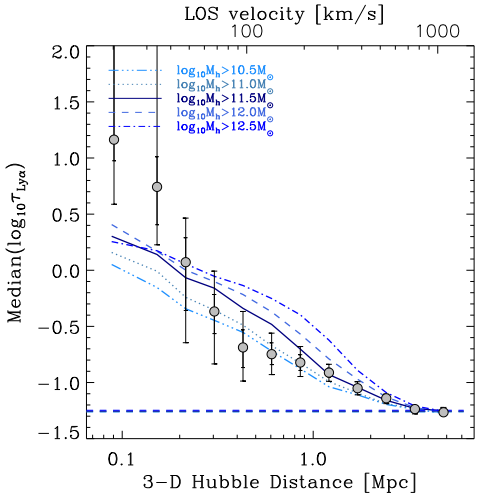

Figure 4.7 – Median $\log_{10}(\tau_{\mathrm{Ly}\alpha})$ as a function of proper distance from galaxy haloes in the 100 h^{-1} cMpc *REF* simulation. Curves represent different mass bins, as indicated in the legend, while black symbols with 1σ and 2σ error bars show the results from the observations. We added redshift errors to galaxy positions in simulations (see text for more details).

4.4 Redshift space anisotropies

Rakic et al. (2011) report on two types of redshift space anisotropies in the observed 2-D Lyα absorption maps. At small impact parameters ($\lesssim 200$ kpc) the absorption signal is elongated along the LOS, which is likely a result of gas peculiar velocities of $\approx 200\,\mathrm{km\,s^{-1}}$, and errors in galaxy redshifts ($\approx 125\,\mathrm{km\,s^{-1}}$). On the other hand, at large separations from galaxies (≈ 1.5 Mpc) the absorption appears compressed along the LOS, which probably reflects large-scale gas infall into the potential wells populated by the observed galaxies.

Here we use simulated observations to examine the origin of the observed redshift space anisotropies. Figure 4.8 shows 2-D absorption maps centered on haloes with masses higher than the minimum mass inferred in the previous section, i.e. $\mathrm{M_h} > 10^{11.5}\,\mathrm{M_\odot}$, for 4 cases: *i)* default case, i.e. redshift errors of $\sigma = 60\,\mathrm{km\,s^{-1}}$ for 10% of galaxy redshifts, and $\sigma = 125\,\mathrm{km\,s^{-1}}$ for the remaining 90% of redshifts, and taking into account peculiar velocities, *ii)* no redshift errors, *iii)* ignoring peculiar velocities, and *iv*) a number of sightlines per distance bin identical to the observations of Rakic et al. (2011).

Comparing the middle left and right panel of Figure 4.8 we see that the effect of redshift errors is to wash out the signal along the LOS.

The bottom left panel shows the case where we ignore peculiar velocities. The absorption enhancement is more isotropic around the halo positions. At small impact parameters ($\lesssim 200$ pkpc), the absorption is much reduced, demonstrating that peculiar velocities strongly enhance the small-scale absorption excess. In addition, comparison with the middle left panel suggests that the large-scale ($\gtrsim 1.5$ Mpc) compression along the LOS is due to large-scale infall. This is the first observation of gas collapse into large-scale potential wells. We just note here that ignoring both peculiar velocities and redshift errors results in a map with axisymmetric absorption.

In the bottom right panel we limit the number of sightlines per distance bin to match the observations. The resulting map is noisier in comparison with the previous panels with simulated maps, but the redshift space distortions seen in the first panel are also clearly visible in this panel.

A more quantitative comparison is provided by Figures 4.9 and 4.10 which show cuts along the LOS and in transverse direction, respectively, for three different cases. The top left panel of Figure 4.9 makes it very clear that the simulations underpredict the amount of absorption for impact parameters smaller than ≈ 100 kpc. Note, however, that a simple "χ by eye" would strongly overestimate the significance of the discrepancy because the points are strongly correlated in the line of sight direction (Rakic et al. 2011). Both figures show that redshift errors smooth the signal along the LOS, on scales $\lesssim 10^2\,\mathrm{km\,s^{-1}}$. The curves for the case where we do not take peculiar velocities into account lie below the default curves for velocity separations $\lesssim 150\,\mathrm{km\,s^{-1}}$, and above them at larger velocity separations. The increased

optical depth closer to galaxies could be due to large-scale infall of gas enhancing absorption through "filling" in redshift space. Another possibility is that the enhanced absorption is due to lines getting broadened due to large scale galactic outflows, which would also significantly affect our median statistics. While there is some ambiguity at small impact parameters, the evacuation of absorption on large scales is likely due to large scale gas infall.

In Figure 4.11 we add different amounts of scatter to the galaxy redshifts. Large redshift errors smooth the absorption signal more along the LOS. The bottom panels show cases with redshift errors of $\sigma = 300$ and $400\,\mathrm{km\,s^{-1}}$, where instead of compression along the LOS relative to the direction transverse to the LOS, we see elongation. This suggests that the errors in galaxy redshifts have to be $< 200\,\mathrm{km\,s^{-1}}$ to study large scale-gas infall into the potential wells of star-forming galaxies.

4.5 Summary & Conclusions

Several observations have shown that the absorption of the light from background QSOs is enhanced at the wavelength of H I Lyα when a sightline passes within several pMpc from a galaxy. We compared the observed Lyα absorption distribution around star-forming galaxies at $z \approx 2.36$ from Rakic et al. (2011) with cosmological SPH simulations in order to statistically constrain the total halo masses of the observed galaxy population, and to explain the observed redshift space distortions.

The most important conclusions of this study are:

- Using cosmological SPH simulations from the OWLS suite of models we derive the minimum halo mass of $\log_{10}M_{\rm min} = 11.6^{+0.20+0.50}_{-0.20-0.60}\,\mathrm{M_\odot}$ for the *REF* model, in good agreement with the estimates from the clustering analysis (Conroy et al. 2008) and Trainor et al. (2011, in preparation) performed on the same galaxy population.
- Our method is robust to changes in feedback prescriptions as demonstrated by comparison with the *AGN* model in which galaxies eject large amounts of gas at the redshift of interest here. The implied minimum mass of $\log_{10}M_{\rm min} = 11.9^{+0.20+0.30}_{-0.30-0.70}\,\mathrm{M_\odot}$, although 0.3 dex higher, is consistent with the *REF* model within 1σ.
- The minimum halo mass inferred from comparison with the *MILL* simulation ($\log_{10}M_{\rm min} = 11.7^{+0.05+0.30}_{-0.40-0.90}\,\mathrm{M_\odot}$) is consistent with that required by the *WML4* model ($\log_{10}M_{\rm min} = 11.4^{+0.50+0.80}_{-0.10-0.10}\,\mathrm{M_\odot}$), which suggests that our method is not very sensitive to differences in cosmological parameters (WMAP1 vs. WMAP3).
- If we consider only a cut along the LOS for impact parameters $\lesssim 100$ pkpc, then we infer a mass of $\log_{10}M_{\rm min} = 11.6^{+0.50+0.50}_{-0.05-0.05}\,\mathrm{M_\odot}$, which is almost identical to the one obtained from the full 2-D map (impact parameters $\lesssim 2$ pMpc). This is very encouraging for future narrow

field QSO-galaxy surveys (e.g. the one planned with the VLT/MUSE), where one will be able to estimate halo masses of Lyα emitters with a single telescope pointing, without the need for a wide field mosaic.

- The observed elongation of the absorption signal of $\approx 200\,\mathrm{km\,s^{-1}}$ at small impact parameters is a product of uncertainties in galaxy redshifts, observed to be $\approx 125\,\mathrm{km\,s^{-1}}$, and the peculiar motions of gas in and around galaxy haloes.
- The compression of the signal on large scales is a result of gas infall into potential wells occupied by galaxies. To observe this infall, the accuracy of galaxy redshifts has to be better than $\sim 200\,\mathrm{km\,s^{-1}}$, as larger redshift errors smooth the absorption signal along the LOS, disguising the compression signature.

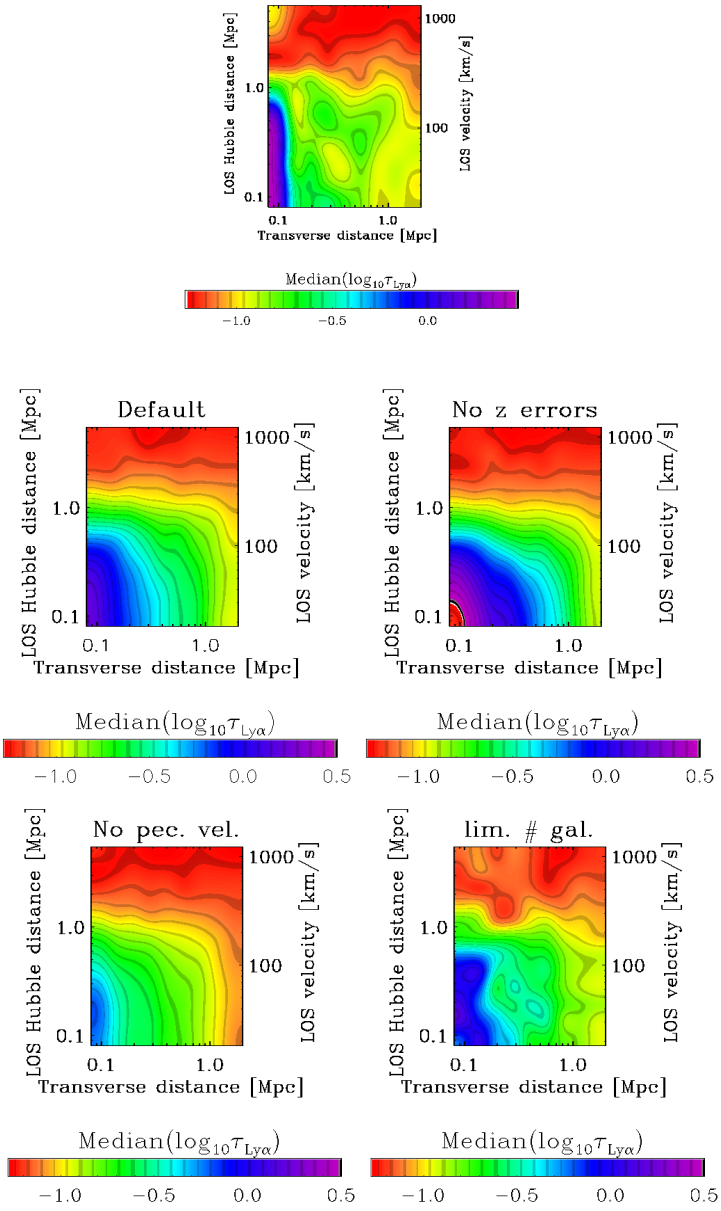

Figure 4.8 – 2-D Lyα absorption maps for haloes with $M_{\rm h} > 10^{11.5}\,{\rm M}_{\odot}$ at $z = 2.25$ in the 50 h^{-1} cMpc *REF* simulation. Top panel: observations of Rakic et al. (2011). Middle left panel: default case (errors in galaxy redshifts, and taking into account peculiar velocities). Middle right panel: no redshift errors. Lower left panel: ignoring peculiar velocities. Lower right panel: number of galaxies per impact parameter bin matches observations of Rakic et al. (2011). Redshift errors increase redshift space distortions on small scales and decrease the signal, while peculiar velocities act to compress signal along the LOS on large scales, elongate it along the LOS for small impact parameters, and increase the signal.

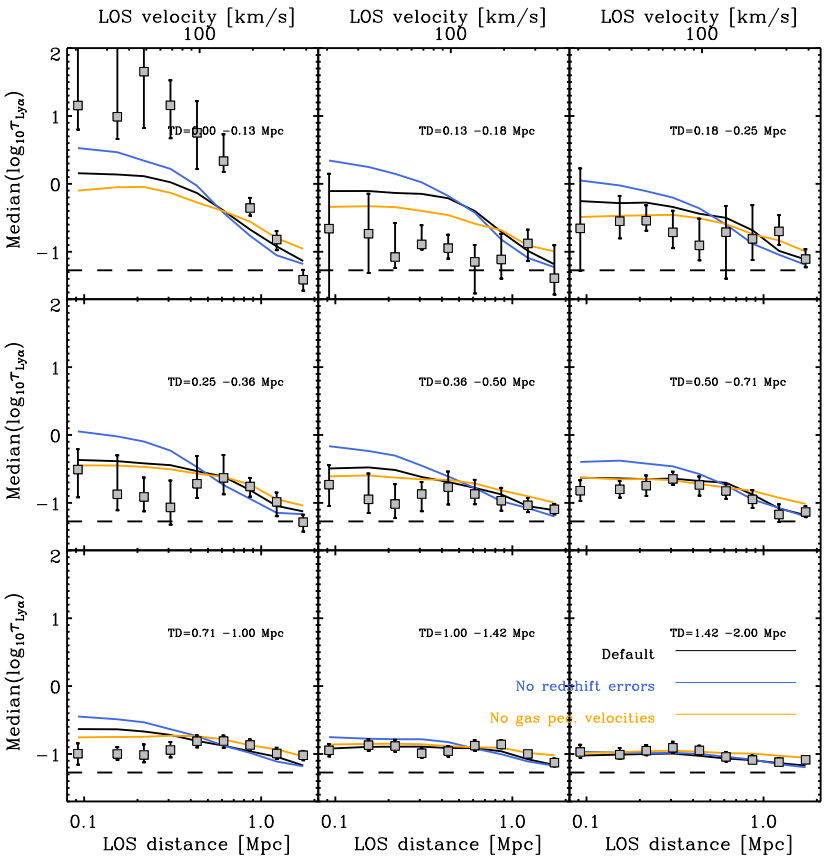

Figure 4.9 – Cuts along the LOS through panels of Figure 4.8 ($M_h > 10^{11.5}$ $M_\odot$). The gray symbols show the observations of Rakic et al. (2011). The horizontal dashed line indicates the median optical depth of all pixels.

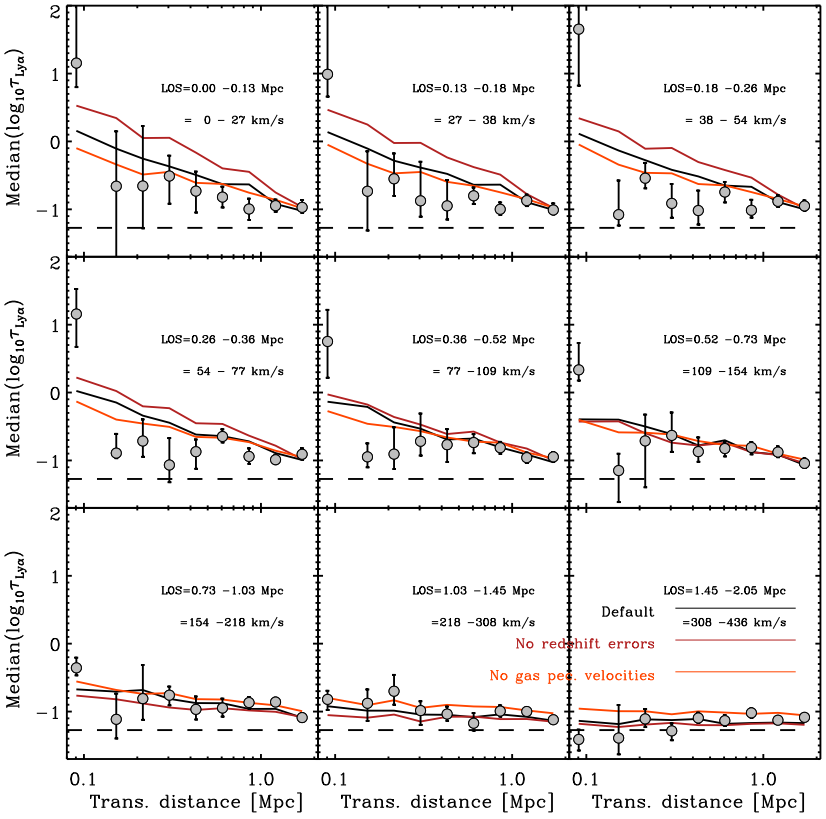

Figure 4.10 – Similar to Figure 4.9, but showing cuts in transverse direction through panels of Figure 4.8 ($M_h > 10^{11.5}\ M_\odot$).

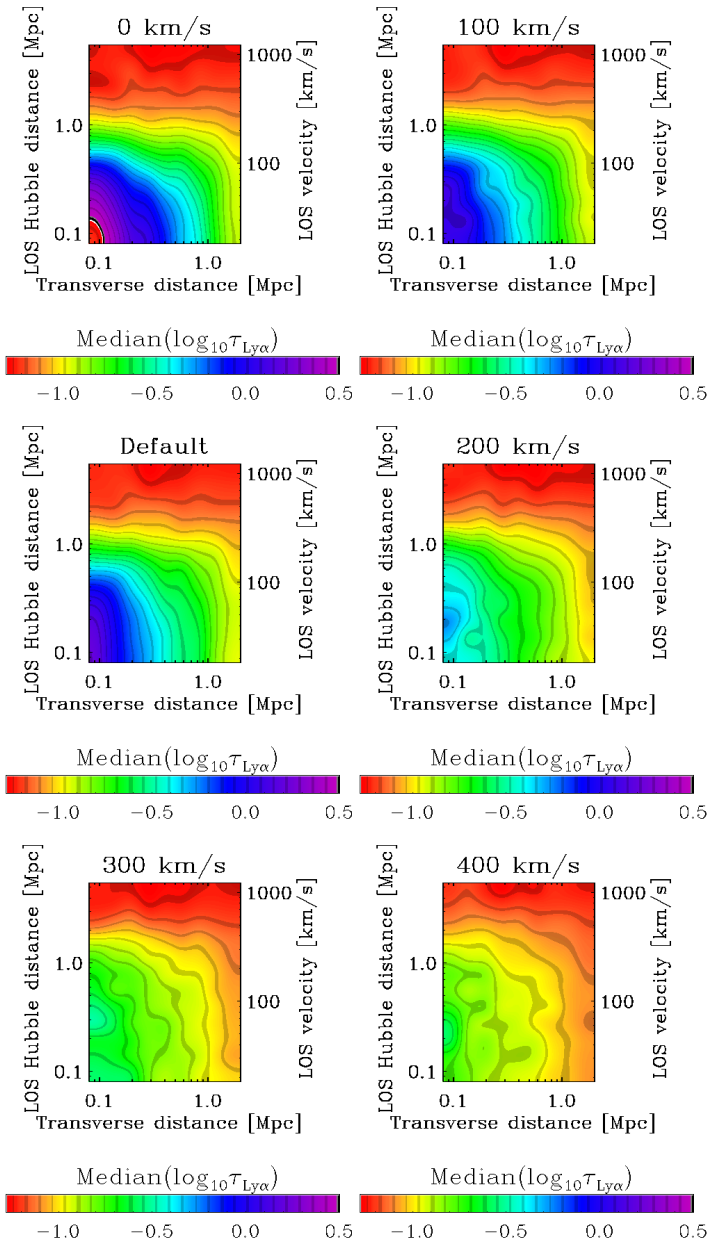

Figure 4.11 – Similar to Figure 4.8 but adding different levels or errors in galaxy redshifts: $\sigma = 0$, 100, default redshift errors (described in the text), 200, 300, and 400 km s^{-1}, from left to right, and from top to bottom. Adding errors with $\sigma \gtrsim 200\,\mathrm{km\,s^{-1}}$ masks the compression of the absorption distribution along the LOS relative to that transverse to the LOS.

References

Adelberger K. L., Steidel C. C., Giavalisco M., Dickinson M., Pettini M., Kellogg, M., 1998, ApJ, 505, 18
Adelberger K. L., Steidel C. C., Shapley A. E., Pettini M., 2003, ApJ, 584, 45
Adelberger K. L., Shapley A. E., Steidel C. C., Pettini M., Erb D. K., Reddy N. A., 2005, ApJ, 629, 636
Adelberger K. L., Steidel C. C., Pettini M., Shapley A. E., Reddy N. A., Erb D. K. 2005, ApJ, 619, 697
Bacon R. et al., 2010, Proc. SPIE, 7735, 7
Booth, C. M., Schaye, J., 2009, MNRAS, 398, 53
Booth, C. M., Schaye, J., 2010, MNRAS, 405, 1
Chabrier, G., 2003, PASP, 115, 763
Chen H.-W., Lanzetta K. M., Webb J. K., Barcons X., 1998, ApJ, 498, 77C
Chen H.-W., Lanzetta K. M., Webb J. K., 2001, ApJ, 556, 158
Croft R. A. C., Hernquist L., Springel V., Westover M., White M., 2002, ApJ, 580, 634
Conroy, C., Wechsler, R. H., Kravtsov, A. V., 2006, ApJ, 668, 826
Conroy C., Shapley A. E., Tinker J. L., Santos M. R., Lemson G.
Crighton N. et al., 2010 MNRAS, 414, 28
Cole, S., Kaiser, N., MNRAS, 237, 1127
Dalla Vecchia, C., Schaye, J., 2008, MNRAS, 387, 1431
Dolag, K., Borgani, S., Murante, G., Springel, V., 2009, MNRAS, 399, 497
Faucher-Giguère, C.-A., Lidz, A., Zaldarriaga, M., Hernquist, L., 2008, ApJ, 673, 39
Franx, M., Labbé, I., Rudnick, G., van Dokkum, P. G., Daddi, E., Förster Schreiber, N. M., Moorwood, A., Rix, H.-W., Röttgering, H., van der Wel, A., van der Werf, P., van Starkenburg, L., 2003, ApJ, 587, 79
Gavazzi, R., Treu, T., Rhodes, J. D., Koopmans, L. V. E., Bolton, A. S., Burles, S., Massey, R. J., Moustakas, L. A., 2007, ApJ, 667, 176
Gunn, J. E., Peterson, B. A., 1965, ApJ, 142, 1633
Haardt F., Madau P., 2001, in Neumann D. M., Tran J. T. V., eds, Clusters of Galaxies and the High Redshift Universe Observed in X-rays Modelling the UV/X-ray cosmic background with CUBA, arXiv: 0106018
Haas, M. R., Schaye, J., Jeeson-Daniel, A., 2011, arXiv: 1103.0547
Kaiser, N., 1984 ApJ, 284, 9
Kaiser, N., Squires, G., 1993, ApJ, 404, 441
Kim, Y.-R., Croft, R. A. C., 2008, MNRAS, 387, 377
Komatsu E. et al., 2011, ApJS, 192, 18
Mandelbaum, R., Seljak, U., Kauffmann, G., Hirata, C. M., Brinkmann, J., 2006, MNRAS, 368, 715
McCarthy, I. G., Schaye, J., Bower, R. G., Ponman, T. J., Booth, C. M., Dalla Vecchia, C., Springel, V., 2011, MNRAS, 412, 1965
More, S., van den Bosch, F. C., Cacciato, M., Skibba, R., Mo, H. J., Yang, X., 2011, MNRAS, 410, 210
Motl, P. M., Hallman, E. J., Burns, J. O., Norman, M. L., 2005, ApJ, 623, 63
Penton S. V., Stocke J. T., Shull J. M., 2002, ApJ, 565, 720
Prochaska, J. X., Weiner, B., Chen, H. -., Mulchaey, J. S., Cooksey, K. L., 2011, arXiv: 1103.1891

Quadri, R., van Dokkum, P., Gawiser, E., Franx, M., Marchesini, D. , Lira, P., Rudnick, G., Herrera, D., Maza, J., Kriek, M., Labbé, I., Francke, H., 2007, ApJ, 654, 138
Rakic et al., 2011, in preparation
Reddy, N. A., Steidel, C. C., Pettini, M., Adelberger, K. L., Shapley, A. E., Erb, D. K., Dickinson, M., 1998, ApJS, 175, 48
Reiprich, T. H., Böhringer, H., ApJ, 567, 716
Schaye, J., 2001, ApJ, 559, 507
Schaye J., Rauch M., Sargent W. L. W., Kim T.-S., 2000, ApJ, 541, 1
Schaye J., Dalla Vecchia, C., 2008, MNRAS, 383.1210
Schaye, J., Dalla Vecchia, C., Booth, C. M., Wiersma, R. P. C., Theuns, T., Haas, M. R., Bertone, S., Duffy, A. R., McCarthy, I. G., van de Voort, F., 2010, MNRAS, 402, 1536
Spergel et al., 2007, ApJS, 170, 377
Springel, V., White, S. D. M., Tormen, G., Kauffmann, G., 2001, MNRAS, 328, 726
Springel V., 2005, MNRAS, 364, 1105
Springel, V. et al., 2005, Nature, 435, 629
Steidel, C. C., Shapley, A. E., Pettini, M., Adelberger, K. L., Erb, D. K., Reddy, N. A., Hunt, M. P., 2004, ApJ, 604, 534
Steidel C. C., Erb D. K., Shapley A. E., Pettini M., Reddy N., Bogosavljević M., Rudie G. C., Rakic O., 2010, ApJ, 717, 289
Sunyaev, R. A., Zeldovich, Y. B., CoASP, 4, 173
Theuns T., Leonard A., Efstathiou G., Pearce F. R., Thomas P. A., 1998, MNRAS, 301, 478
van de Voort, F., Schaye, J., Booth, C. M., Haas, M. R., & Dalla Vecchia, C. 2011, MNRAS, 414, 2458
Vogt S. S., Allen S. L., Bigelow B. C., Bresee L., Brown B., Cantrall T., Conrad A., Couture M., 1994, Proc. SPIE, 2198, 362
Wiersma, R. P. C., Schaye, J., Smith, B. D., 2009. MNRAS, 393, 99
Wiersma, R. P. C., Schaye, J., Theuns, T., Dalla Vecchia, C., Tornatore, L., 2009, MNRAS, 399, 574
Zwicky, F., 1937, ApJ, 86, 217

4.A Convergence Tests

Figure 4.12 shows the mass resolution test for the 50 h^{-1} cMpc *REF* simulation, performed with 128^3, 256^3, and 512^3 particles. The resulting median $\log_{10}(\tau_{\mathrm{Ly}\alpha})$ curves as a function of proper distance from the galaxies are consistent with each other for all but the highest mass bin. In the highest mass bin the resulting curve for the simulation with the poorest resolution is below the curves for simulations with higher resolution, but the simulations with 256^3, and 512^3 particles give consistent results. Therefore, we can conclude that the simulation results are converged with respect to the particle mass.

Figure 4.13 shows the results for the 50 h^{-1} cMpc *REF* simulation with 256^3, and 100 h^{-1} cMpc *REF* simulation with 512^3 particles. In this case the particle masses in the two simulations are the same, but the simulation

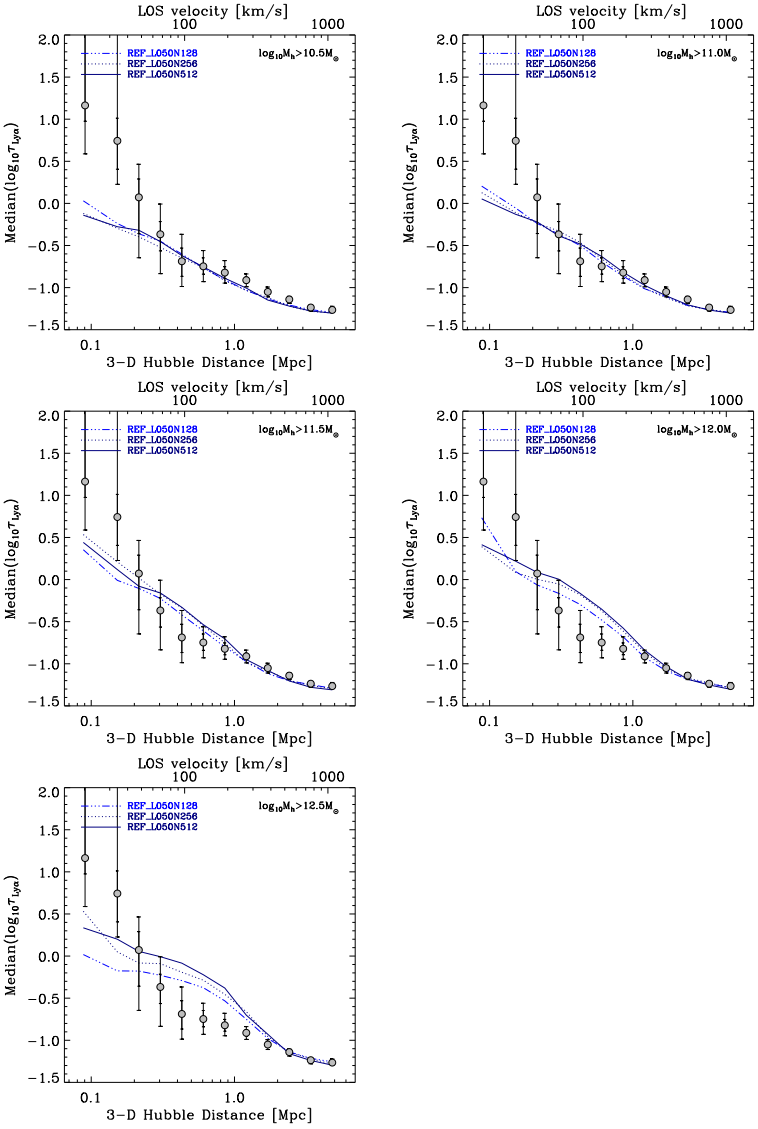

Figure 4.12 – Median $\log_{10}(\tau_{\mathrm{Ly}\alpha})$ as a function of proper distance from galaxy haloes in the 50 h^{-1} cMpc *REF* simulations, with 128^3, 256^3, and 512^3 particles. Each panel shows the results for a different mass range, as indicated in the legend, while grey symbols with 1σ and 2σ error bars show the results from the observations. We added errors to galaxy positions in simulations (see text for more details).

volume is changed. The median optical depth curves show that the results are converged with respect to the box size.

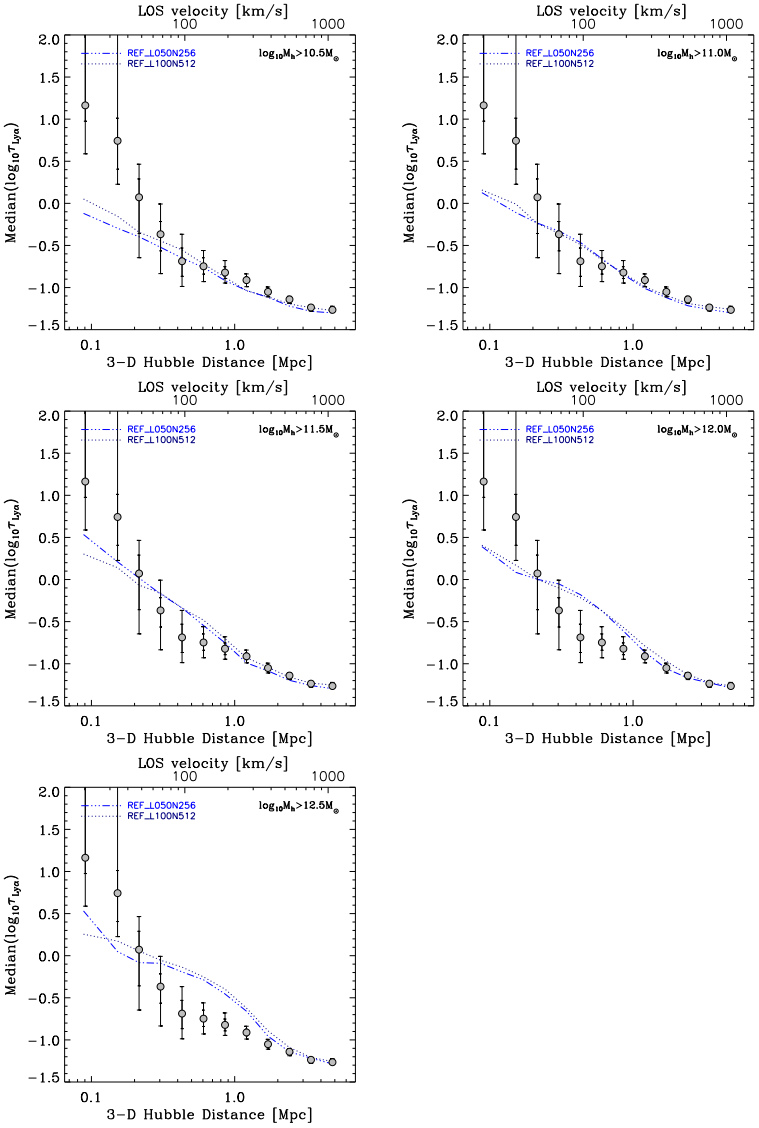

Figure 4.13 – Median $\log_{10}(\tau_{\mathrm{Ly}\alpha})$ as a function of proper distance from galaxy haloes in the 50 h^{-1} cMpc *REF* simulation with 256^3, and 100 h^{-1} cMpc *REF* simulation with 512^3 particles. Each panel shows the results for a different mass range, as indicated in the legend, while grey symbols with 1σ and 2σ error bars show the results from the observations. We added errors to galaxy positions in simulations (see text for more details).